JM PAPERS

Self-propulsion of an elliptical phoretic disk emitting solute uniformly

Guangpu Zhu[1] **and Lailai Zhu**[1,†]

[1]Department of Mechanical Engineering, National University of Singapore 117575, Republic of Singapore

Self-propulsion of chemically active droplets and phoretic disks has been studied widely; however, most research overlooks the influence of disk shape on swimming dynamics. Inspired by experimentally observed prolate composite droplets and elliptical camphor disks, we employ simulations to investigate the phoretic dynamics of an elliptical disk that emits solutes uniformly in the creeping flow regime. By varying the disk's eccentricity e and the Péclet number Pe, we distinguish five disk behaviours: stationary, steady, orbiting, periodic and chaotic. We perform a linear stability analysis (LSA) to predict the onset of instability and the most unstable eigenmode when a stationary disk transitions spontaneously to steady self-propulsion. In addition to the LSA, we use an alternative approach to determine the perturbation growth rate, illustrating the competing roles of advection and diffusion. The steady motion features a transition from a puller-type to a neutral-type swimmer as Pe increases, which occurs as a bimodal concentration profile at the disk surface shifts to a polarized solute distribution, driven by convective solute transport. An elliptical disk achieves an orbiting motion through a chiral symmetry-breaking instability, wherein it repeatedly follows a circular path while simultaneously rotating. The periodic swinging motion, emerging from a steady motion via a supercritical Hopf bifurcation, is characterized by a wave-like trajectory. We uncover a transition from normal diffusion to superdiffusion as eccentricity e increases, corresponding to a random-walking circular disk and a ballistically swimming elliptical counterpart, respectively.

Key words: propulsion, swimming/flying

1. Introduction

Synthetic microswimmers have attracted much attention owing to their promising potential in biomedical and bioengineering applications (Sitti *et al.* 2015), e.g. detection and collection of metal ions (Ban *et al.* 2018), targeted controlled drug delivery

† Email address for correspondence: lailai_zhu@nus.edu.sg

(Kagan *et al.* 2010; Tang *et al.* 2020), and cancer cell microsurgery (Vyskocil *et al.* 2020). Drawing inspiration from the propulsion strategies of microorganisms in nature, various biomimetic swimmers that propel in viscous fluids have been developed (Ghosh & Fischer 2009; Van Oosten, Bastiaansen & Broer 2009; Ahmed *et al.* 2016; Soto *et al.* 2021). Unlike their biological counterparts, these synthetic microswimmers are commonly powered by external forces or torques coming from the electric, optic, acoustic or magnetic fields (Rao *et al.* 2015; Palagi *et al.* 2016; Koleoso *et al.* 2020); for example, a sperm-mimicking microswimmer with a flexible filament actuated magnetically (Dreyfus *et al.* 2005). Despite the rapid development of externally actuated microswimmers, some practical difficulties, such as miniaturization and manufacturing of moving parts for certain swimmers, have limited their applications in realistic scenarios (Ebrahimi *et al.* 2021; Joh & Fan 2021; Li *et al.* 2022).

Unlike externally actuated swimmers, chemically active swimmers convert chemical energy stored internally or extracted from their surroundings into motion (Moran & Posner 2017). They can be classified broadly by whether their surface properties, e.g. surface activity and mobility, are anisotropic or isotropic. A classical anisotropic swimmer is the Janus colloid, e.g. the autophoretic Au–Pt Janus colloid (Paxton *et al.* 2004). Typically, the chemically patterned asymmetric colloid features two distinct compartments, each composed of a different material or bearing diverse functional groups (Lattuada & Hatton 2011), which enables asymmetric chemical reactions at the surface. The inherent asymmetry allows it to self-generate a concentration gradient, which drives a slip flow inducing net phoretic propulsion, as revealed by experimental (Paxton *et al.* 2006; Duan *et al.* 2015; Campbell *et al.* 2019), theoretical (Golestanian, Liverpool & Ajdari 2007; Brady 2011; Datt *et al.* 2017; Nasouri & Golestanian 2020*a*) and numerical (Popescu *et al.* 2010; Sharifi-Mood, Mozaffari & Córdova-Figueroa 2016; Kohl *et al.* 2023) studies. The Janus swimmer is typically micro-scale or even smaller, and its phoretic motion is Brownian (Michelin 2023). Its self-propulsion requires a built-in asymmetry in the surface properties. This requirement presents a challenge to the controlled and reproducible manufacturing of Janus colloids, hence hindering their high-throughput production (Su *et al.* 2019).

Chemically isotropic swimmers are much easier to manufacture compared to their anisotropic counterparts. A simple and typical representative of such swimmers is a chemically active droplet, e.g. a water droplet dissolving slowly in a surfactant-saturated oil phase, which has been researched extensively since its first experimental realization (Izri *et al.* 2014). These active droplets are generally larger than the Janus microswimmers and have typical radii ranging from 10 to 100 μm. Active droplets consist mainly of reacting droplets (Thutupalli & Herminghaus 2013; Kasuo *et al.* 2019; Suematsu *et al.* 2019) and solubilizing droplets (Peddireddy *et al.* 2012; Seemann, Fleury & Maass 2016; Hokmabad *et al.* 2021). The former involve chemical reactions producing or changing surfactant molecules at their surface, while the latter feature a micellar dissolution into the surfactant-saturated ambient phase. In both instances, spatial modulation of the surface tension at the droplet interface may potentially induce Marangoni flows. Such droplets do not rely on built-in asymmetry like the Janus colloids, but instead attain self-propulsion via an instability spontaneously breaking the spatial symmetry. This instability arises from the nonlinear convective transport of solute species by fluid flow, resulting from Marangoni and/or phoretic effects produced by local chemical gradients surrounding the droplet (Morozov & Michelin 2019*a*; Picella & Michelin 2022). Besides the active droplet, another class of chemically isotropic swimmers consists of camphor disks that surf at a liquid–air interface (Tomlinson 1862; Nakata *et al.* 2006; Suematsu *et al.* 2010). In this

scenario, camphor molecules dissolved from the disk diffuse into the interface and further the subsurface liquid, and the Marangoni flows resulting from the solute gradient drive the disk to propel (Matsuda *et al.* 2016; Boniface *et al.* 2021). Notably, the Marangoni flows generated by active droplets are solely at their surface, while those triggered by camphor disks are along the air–liquid interface and depend significantly on the depth of the subsurface liquid (Matsuda *et al.* 2016; Michelin 2023).

Active droplets exhibit complex and tunable motion as a result of the nonlinear physico-chemical hydrodynamics (Hokmabad *et al.* 2021; Li 2022), characterized by the Péclet number *Pe* as the ratio of flow advection to solute diffusion. At low *Pe*, an isolated droplet remains stationary. Morozov & Michelin (2019*b*) identified the critical Péclet number for an undeformable droplet through a stability analysis, beyond which an unstable dipolar mode of hydrodynamics emerges, driving the spontaneous propulsion of the droplet. This critical *Pe* is unchanged when the droplet internal flow is neglected, as identified for a chemically isotropic spherical particle initially proposed to mimic an active droplet (Michelin, Lauga & Bartolo 2013). Besides, the critical *Pe* determined for a two-dimensional (2-D) undeformable droplet (Li 2022) is also consistent with that for a phoretic disk (Hu *et al.* 2019). Near the critical *Pe*, the dipolar mode is the only unstable one (Schnitzer 2023; Peng & Schnitzer 2023). However, higher-order modes, e.g. the quadrupolar mode, become successively unstable with increasing *Pe*, leading to the possible coexistence of multiple unstable modes with different polar symmetries (Morozov & Michelin 2019*a*; Hokmabad *et al.* 2021). Accordingly, the active droplet sequentially exhibits quasi-ballistic, unsteady curvilinear and even chaotic motions (Krüger *et al.* 2016; Suga *et al.* 2018; Hokmabad *et al.* 2021; Li 2022) as *Pe* grows. Analogous behaviours of 2-D (Hu *et al.* 2019, 2022) and three-dimensional (3-D) isotropic phoretic particles have also been observed (Chen *et al.* 2021; Hu *et al.* 2022; Kailasham & Khair 2022). Besides an isolated unbounded droplet/particle, the effect of nearby boundaries/fluid interfaces (Jin *et al.* 2018; Malgaretti, Popescu & Dietrich 2018; Thutupalli *et al.* 2018; de Blois *et al.* 2019; Lippera *et al.* 2020*b*; Desai & Michelin 2021; Dey *et al.* 2022; Picella & Michelin 2022), that of an ambient flow (Yariv & Kaynan 2017; Dwivedi *et al.* 2021; Dey *et al.* 2022), and interaction among multiple droplets/particles (Jin, Krüger & Maass 2017; Lippera, Benzaquen & Michelin 2020*a*; Meredith *et al.* 2020; Nasouri & Golestanian 2020*b*; Hokmabad *et al.* 2022; Wentworth *et al.* 2022; Yang *et al.* 2023) have been investigated. One specific point that we should mention is that an active droplet/particle near boundaries (Daddi-Moussa-Ider, Vilfan & Golestanian 2022), fluid interfaces (Malgaretti *et al.* 2018) or another droplet/particle (Michelin & Lauga 2015) generally exploits geometric asymmetry to propulsion, which is significantly distinct from an isolated droplet/particle.

Most of the active droplets observed in experiments were weakly deformed and remained spherical; one exception is the recent work by Hokmabad *et al.* (2019), reporting the self-propulsion of a prolate composite droplet along its minor axis, with that oil droplet trapping two aqueous daughter droplets at the opposing poles of its major axis, suspended in an aqueous surfactant solution. The daughter droplets are submicellar, whereas the external aqueous phase is supramicellar. The micellar dissolution at the external oil–water interface induces a self-sustaining surface tension gradient, driving the droplet motion. Compared to droplets, solid self-propelling swimmers relying on a similar symmetry-breaking mechanism exhibit greater flexibility in shape. Kitahata, Iida & Nagayama (2013) and Iida, Kitahata & Nagayama (2014) investigated experimentally and theoretically the spontaneous motion of an elliptical camphor disk at the air–liquid interface, and found that the disk swam along its minor axis resembling the swimming
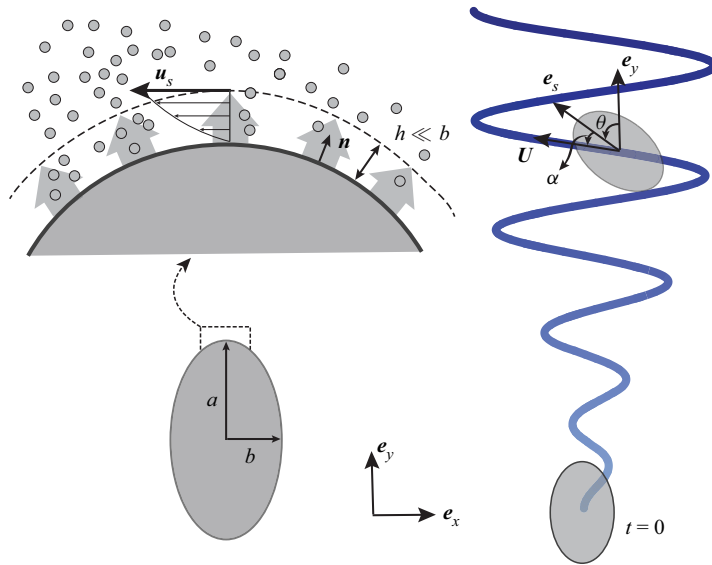
Figure 1. Self-propulsion of an elliptical disk uniformly releasing chemical solutes in a Newtonian solvent, where $\boldsymbol{e}_x, \boldsymbol{e}_y$ denotes the laboratory frame. The disk moves along an undulatory path with translational velocity $\boldsymbol{U}$, and the colour of the path is coded by the time t. The disk orientation $\boldsymbol{e}_s$ coinciding with its major axis deviates from $\boldsymbol{e}_y$ and $\boldsymbol{U}$ by angles θ and α, respectively. The inset shows the induced slip velocity $\boldsymbol{u}_s$ by local solute gradients within a thin boundary layer of thickness $h \ll b$. Here, $\boldsymbol{n}$ denotes the unit normal vector pointing away from the disk surface. All the variables here are dimensionless.

prolate droplet (Hokmabad *et al.* 2019). Shimokawa & Sakaguchi (2022) observed that an elliptical camphor-coated paper disk exhibited spontaneous rotation at a constant angular velocity. Motivated by these non-spherical phoretic swimmers with uniform chemical reactions at their surface, especially Kitahata *et al.* (2013) and Hokmabad *et al.* (2019), here we explore theoretically and numerically, in the creeping flow regime, the instability-driven spontaneous propulsion of an elliptical phoretic disk that releases chemical species uniformly. We perform a linear stability analysis (LSA) to investigate the onset of instability, and direct numerical simulations to explore the swimming behaviour of the phoretic disk.

This paper is organized as follows. We describe the problem set-up, assumptions and governing equations in § 2. The implementation for the LSA is introduced in § 3, followed by § 4 demonstrating numerical and theoretical results. Finally, we conclude our observations and provide some discussion in § 5.

2. Problem set-up, governing equations and methodology

2.1. *Problem set-up and governing equations*

We consider a chemically active elliptical disk emitting or absorbing solute molecules uniformly in an incompressible Newtonian fluid of dynamic viscosity $\bar{\eta}$ (see figure 1). From here on, the bar indicates a dimensional variable unless stated otherwise. The semi-major and semi-minor axes of the disk are $\bar{a}$ and $\bar{b} \leq \bar{a}$, respectively, and $\bar{c}_f = \sqrt{\bar{a}^2 - \bar{b}^2}$ denotes half of its focal length. Hence the disk shape can be characterized by the eccentricity $e = \bar{c}_f / \bar{a}$, which amounts to 0 or approaches 1 as the disk becomes circular or needle-like. We choose the major axis of the disk to denote its orientation $\boldsymbol{e}_s = \sin \theta \, \boldsymbol{e}_x + \cos \theta \, \boldsymbol{e}_y$, which is characterized by its angular deviation from $\boldsymbol{e}_y$.

We now describe the phoretic dynamics of the elliptical disk and the associated governing equations (Anderson 1989; Michelin *et al.* 2013). The disk's surface Γ_d uniformly emits or absorbs solutes at a constant rate $\bar{A}$ (activity), hence

$$\bar{D}\boldsymbol{n} \cdot \nabla\bar{c}|_{\Gamma_d} = -\bar{A}. \tag{2.1}$$

Here, $\bar{c}$ is the solute concentration, $\bar{D}$ denotes the molecular diffusivity of the solute, and $\boldsymbol{n}$ is the unit outward normal at the surface. Positive or negative $\bar{A}$ corresponds to the solute emission or absorption at the disk surface, respectively. The solute interacts with the disk surface through a short-range potential, and here we focus on the classical thin-interaction-layer limit $h \ll \bar{b}$, with h the thickness of the interaction layer. Within this layer, the slip velocity along the disk surface induced by the local tangential solute gradients (Anderson 1989) reads

$$\bar{\boldsymbol{u}}_s|_{\Gamma_d} = \bar{M}\,\nabla_s\bar{c}, \tag{2.2}$$

where $\bar{\boldsymbol{u}}_s$ indicates the slip velocity, $\nabla_s = (\boldsymbol{I} - \boldsymbol{nn}) \cdot \nabla$ is the surface gradient operator, and $\bar{M}$ denotes the phoretic mobility coefficient. The coefficient $\bar{M}$ determines the chemotactic direction of the phoretic swimmer. For active droplets, $\bar{M}$ can be adjusted by tuning the relationship between surface tension and chemical solute, as shown by recent experiments (Wentworth *et al.* 2022): $\bar{M} > 0$ when they are positively correlated, and $\bar{M} < 0$ when negatively correlated. Prior studies (Michelin *et al.* 2013; Hu *et al.* 2019) revealed that spontaneous symmetry-breaking propulsion is present only when $\bar{A}\bar{M} > 0$; in other cases, the disk remains stable. Without loss of generality, our analysis focuses on $\bar{A} > 0$ and $\bar{M} > 0$, but the results will remain in the converse scenarios. Also, we assume that the inertia of both fluid and disk is negligible compared to the viscous force because the Reynolds number *Re* is typically small in the experiments (Peddireddy *et al.* 2012; Maass *et al.* 2016; de Blois *et al.* 2019; Hokmabad *et al.* 2021, 2022; Michelin 2023). Hence the fluid flow surrounding the disk can be described approximately by the Stokes equation.

In the following, we introduce the dimensionless governing equations. We choose $\bar{A}\bar{M}/\bar{D}$, $\bar{b}$ and $\bar{b}\bar{A}/\bar{D}$, respectively, as the characteristic velocity $\bar{\mathcal{V}}$, length and concentration for the non-dimensionalization. All variables below are dimensionless unless specified otherwise. The dimensionless equations for the velocity $\boldsymbol{u}$, pressure p and concentration c are

$$\nabla \cdot \boldsymbol{\sigma} = \boldsymbol{0}, \quad \nabla \cdot \boldsymbol{u} = 0, \tag{2.3a,b}$$

$$\frac{\partial c}{\partial t} + \boldsymbol{u} \cdot \nabla c = \frac{1}{Pe}\,\Delta c, \tag{2.4}$$

where $Pe = \bar{A}\bar{M}\bar{b}/\bar{D}^2$ measures the ratio of flow advection to solute diffusion, and $\boldsymbol{\sigma} = -p\boldsymbol{I} + \nabla\boldsymbol{u} + (\nabla\boldsymbol{u})^{\mathrm{T}}$ is the hydrodynamic stress tensor. At the disk surface, the constant flux boundary condition (2.1) for the concentration reads

$$\boldsymbol{n} \cdot \nabla c|_{\Gamma_d} = -1. \tag{2.5}$$

It is known that (2.4) does not support a steady-state solution within a 2-D infinite domain due to the logarithmic divergence (Sondak *et al.* 2016; Yariv 2017; Kailasham & Khair 2023). To resolve this issue, we consider a circular fluid domain with a finite radius *R*, and

prescribe on its exterior Γ_o that

$$c|_{\Gamma_o} = 0. \tag{2.6}$$

Following Hu *et al.* (2019) and Li (2022), here we set $R = 200$. In fact, we also examine the convergence of numerical results with respect to the domain size R, and reveal that the chosen R is sufficiently large to ensure that the disk motion remains unaffected, as depicted in figure 13 of Appendix C.

We perform numerical simulations in the frame co-moving with the disk centre. Hence the boundary conditions for the velocity at the disk surface Γ_d and the outer boundary Γ_o are

$$\boldsymbol{u}|_{\Gamma_d} = \boldsymbol{u}_s + \boldsymbol{\Omega} \times (\boldsymbol{x}_s - \boldsymbol{x}_c), \tag{2.7a}$$

$$\boldsymbol{u}|_{\Gamma_o} = -\boldsymbol{U}, \tag{2.7b}$$

where $\boldsymbol{u}_s = \nabla_s c$ is the slip velocity at the disk surface, and $\boldsymbol{x}_s$ and $\boldsymbol{x}_c$ denote the coordinates of a general point at the disk surface and the disk centre, respectively. Here, $\boldsymbol{U}$ and $\boldsymbol{\Omega}$ denote the translational and rotational velocities of the disk, respectively, which are determined by the force-free and torque-free conditions (Lauga & Powers 2009)

$$\boldsymbol{F} = \int_{\Gamma_d} \boldsymbol{n} \cdot \boldsymbol{\sigma} \, \mathrm{d}l = \boldsymbol{0}, \tag{2.8a}$$

$$\boldsymbol{T} = \int_{\Gamma_d} (\boldsymbol{x}_s - \boldsymbol{x}_c) \times (\boldsymbol{n} \cdot \boldsymbol{\sigma}) \, \mathrm{d}l = \boldsymbol{0}. \tag{2.8b}$$

In other words, the total force and torque exerted on the disk swimmer are zero. The initial condition is zero velocity, pressure and concentration within the domain. Equations (2.3a,b)–(2.8) form the complete set of governing equations for an elliptical phoretic disk in the frame co-moving with the disk.

2.2. *Numerical method*

We solve numerically the governing equations, using a finite-element method solver implemented in the commercial package COMSOL Multiphysics (I-Math, Singapore). We adopt the moving mesh technique to tackle the deformation of the fluid domain caused by disk rotation. Taylor–Hood and quadratic Lagrange elements are employed to discretize the flow field $(\boldsymbol{u}, p)$ and the concentration c, respectively. The computational domain is discretized by approximately 85 000–127 000 triangular elements, and the mesh is refined locally near the disk. Our COMSOL implementations are validated extensively against several published datasets, as shown in Appendix A.

3. Linear stability analysis

Prior studies reveal that a chemically isotropic disk/droplet possesses a stable stationary state at a sufficiently low *Pe*. As *Pe* grows beyond a critical value, an instability arises, leading the disk/droplet to swim autonomously (Hu *et al.* 2019; Morozov & Michelin 2019b; Li 2022). Our numerical results indicate that the elliptical disk here exhibits analogous behaviour, hence we conduct an LSA to examine the onset of instability at a critical Péclet number $Pe_c^{(1)}$.

We first decompose the space- (x) and time-dependent state variables (c, u, p) into the sum of a base state and a perturbation state as

$$c(x, t) = c_b(x) + c'(x, t), \qquad (3.1a)$$

$$u(x, t) = u_b(x) + u'(x, t), \qquad (3.1b)$$

$$p(x, t) = p_b(x) + p'(x, t), \qquad (3.1c)$$

where the subscript b denotes base-state fields, and the primed variables are infinitesimal perturbations. The base state can be obtained numerically. By substituting (3.1) into (2.3a,b) and (2.4), and retaining linear terms, we obtain

$$\nabla \cdot \sigma' = 0, \quad \nabla \cdot u' = 0, \qquad (3.2a,b)$$

$$\frac{\partial c'}{\partial t} + u_b \cdot \nabla c' + u' \cdot \nabla c_b = \frac{1}{Pe} \Delta c'. \qquad (3.3)$$

Note that $u_b(x) = 0$ for a stationary circular disk, while for its elliptical counterpart, $u_b(x) \neq 0$ due to the anisotropic concentration distribution at the disk surface (see figure 6a). The perturbations are assumed to vary exponentially in time with a complex growth rate $\lambda = \lambda_r + i\lambda_i$, i.e.

$$c'(x, t) = \hat{c}(x) \exp(\lambda t), \qquad (3.4a)$$

$$u'(x, t) = \hat{u}(x) \exp(\lambda t), \qquad (3.4b)$$

$$p'(x, t) = \hat{p}(x) \exp(\lambda). \qquad (3.4c)$$

Consequently, (3.2a,b) and (3.3) can be reformulated to

$$\nabla \cdot \hat{\sigma} = 0, \quad \nabla \cdot \hat{u} = 0, \qquad (3.5a,b)$$

$$\lambda \hat{c} + u_b \cdot \nabla \hat{c} + \hat{u} \cdot \nabla c_b = \frac{1}{Pe} \Delta \hat{c}. \qquad (3.6)$$

By expanding the translational and rotational velocities similarly, we arrive at $U = U_b + \hat{U} \exp(\lambda t)$ and $\Omega = \Omega_b + \hat{\Omega} \exp(\lambda t)$. Substituting these with (3.1) into (2.5)–(2.7) enables us to derive the boundary conditions for $\hat{c}$ and $\hat{u}$ at the disk surface and outer boundary:

$$n \cdot \nabla \hat{c}|_{\Gamma_d} = 0, \quad \hat{c}|_{\Gamma_o} = 0, \qquad (3.7)$$

$$\hat{u}|_{\Gamma_d} = \nabla_s \hat{c} + \hat{\Omega} \times (x_s - x_c), \quad \hat{u}|_{\Gamma_o} = -\hat{U}. \qquad (3.8)$$

Note that U_b and Ω_b disappear in (3.8), corresponding to a stationary disk of the base state. The force-free and torque-free conditions still hold as

$$\hat{F} = \int_{\Gamma_d} n \cdot \hat{\sigma} \, dl = 0, \qquad (3.9a)$$

$$\hat{T} = \int_{\Gamma_d} (x_s - x_c) \times (n \cdot \hat{\sigma}) \, dl = 0. \qquad (3.9b)$$

Equations (3.5a,b)–(3.9) define an eigenvalue problem. The stability of the base state is determined by the eigenvalue with the largest real part λ_r^0, namely the leading eigenvalue, and the corresponding perturbations $(\hat{u}, \hat{p}, \hat{c})^{\mathrm{T}}$ are called leading eigenmodes. The base
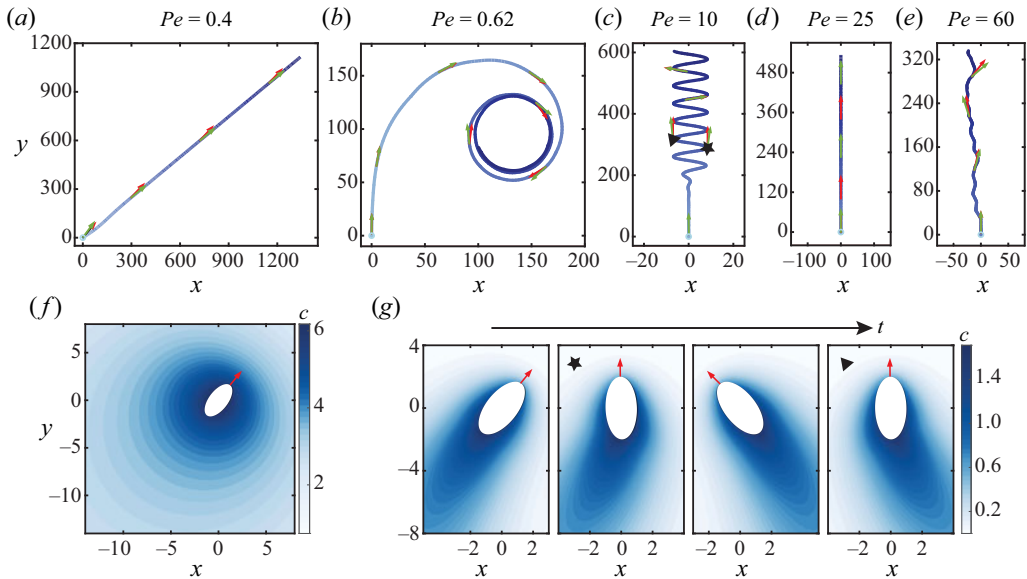
Figure 2. An elliptical disk of eccentricity $e = 0.87$ follows typical trajectories depending on *Pe*: (*a*) steady, (*b*) orbiting, (*c*) periodic, (*d*) steady, and (*e*) chaotic. The colour of a trajectory is coded by the time t. Green and red arrows denote the direction of the translational velocity U and the disk orientation e_s, respectively. (*f*) Polarized concentration distribution with respect to e_s at $Pe = 0.4$. (*g*) Periodic pendulum-like swinging of the disk at $Pe = 10$ in the frame co-moving with its centre. The star and triangle symbols marked in (*g*) denote the two distinct moments when the disk reaches the peak and trough of its trajectory, respectively, as shown in (*c*).

state is stable when $\lambda_r^0 < 0$, but unstable when $\lambda_r^0 > 0$. The Péclet number at which $\lambda_r^0 = 0$ is precisely the critical Péclet number $Pe_c^{(1)}$ signifying the transition from a stationary state to steady propulsion. Unless stated otherwise, the eigenvalues mentioned below refer to the leading eigenvalues, and the superscript 0 is omitted for simplicity. We solve the eigenvalue problem with COMSOL using the eigenvalue solver ARPACK. The validation of our approach is demonstrated in Appendix A.

4. Results

4.1. *Diverse behaviours of an elliptical phoretic disk*

By increasing *Pe*, we demonstrate the diverse *Pe*-dependent behaviours of a disk with eccentricity $e = 0.87$. For a sufficiently small *Pe* below a critical value $Pe_c^{(1)}$, the disk undergoes transient rotation before recovering a stationary state. When *Pe* goes above $Pe_c^{(1)}$, e.g. $Pe = 0.4$, the stationary state transits into steady propulsion, in which the fore–aft symmetry in the concentration profile is broken (see figure 2*f*), and the resultant concentration polarity induces a rectilinear motion with a constant swimming speed, as depicted in figure 2(*a*). Further increasing *Pe* to 0.62, the directed motion loses its stability, leading to a secondary instability characterized by spontaneous chiral symmetry breaking. Consequently, the disk repeatedly traces a circular path, exhibiting spontaneous rotation (clockwise, in this instance), as depicted in figure 2(*b*). This regime featuring circular trajectory and self-rotation is called the orbiting regime. Hu *et al.* (2019) and Li (2022) observed analogous circular trajectories executed by circular swimmers without
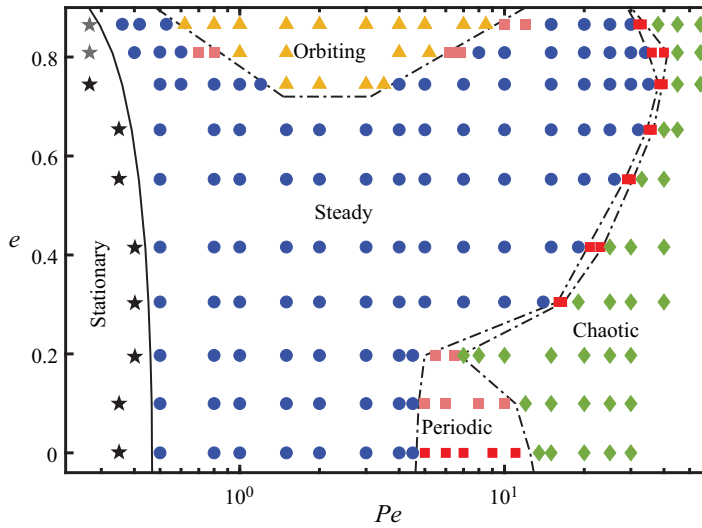
974 A57-8

Figure 3. Phase diagram characterizing the behaviours of an elliptical phoretic disk depending on its eccentricity *e* and the Péclet number *Pe*. It shows five regimes: stationary, steady, orbiting, periodic and chaotic. The solid line denotes the LSA prediction.

self-rotation. At *Pe* = 10, the elliptical disk favours a wave-like trajectory after a transient period of swimming straight forwards (see figure 2*c*). From the viewpoint of the frame co-moving with the disk centre, the disk swings periodically like a pendulum (see figure 2*g*). This swimming behaviour is analogous to that exhibited by an active prolate double-core droplet that moves along an undulatory trajectory (Hokmabad *et al.* 2019). Li (2022) also reported that a high-*Pe* active drop swims along a periodic zigzag trajectory. As *Pe* increases to 25, the elliptical disk surprisingly recovers to steady propulsion, as illustrated in figure 2(*d*). In correspondence, chiral symmetry recovers. Unlike the ballistic motion after rotation at low *Pe*, the disk here travels straight from the onset of instability without any rotation. The steady propulsion becomes unstable at a higher *Pe*, e.g. *Pe* = 33; accordingly, the disk swims straight forwards at an oscillating speed (see figure 12 in Appendix B). Hu *et al.* (2022) and Kailasham & Khair (2022) identified the similar motion of a 3-D isotropic phoretic particle in an axisymmetric set-up, where the particle does not rotate, and the flow and concentration fields are symmetric about an axis parallel to the particle's translational direction. Figure 2(*e*) indicates that the disk enters into a chaotic regime characterized by an erratic trajectory at *Pe* = 60. In contrast to frequent intermittency and random walk occurring in the chaotic regime for a circular disk, as observed by Hu *et al.* (2019), the change of velocity in both direction and magnitude experienced by the elliptical disk is not drastic, yielding a less chaotic trajectory.

Having observed distinct swimming behaviours of a disk with a specific eccentricity at varying *Pe*, we then systematically examine how the eccentricity *e* affects these *Pe*-dependent behaviours. The phase diagram in figure 3 shows that shifts in *Pe*-dependent behaviours of an elliptical disk with *e* below 0.75 resemble those of a circular counterpart (*e* = 0). The elliptical disk executes successively stationary, steady, periodic and chaotic motion with increasing *Pe*. As *e* exceeds 0.75, the disk exhibits richer dynamics: the orbiting motion emerges with broken chiral symmetry. In fact, we have also explored the scenarios at *e* > 0.9, e.g. *e* = 0.96, and observed that the swimming dynamics of the elliptical disk is almost dominated by orbiting and chaotic regimes (not shown here).

These two regimes have been revealed in the current phase diagram, hence the characteristic locomotory modes can be well captured in the range of *e* considered.

We further discern from the phase diagram that the variation of *e* categorizes certain identified swimming patterns into two types. In the stationary or steady swimming regime, the aforementioned observations indicate that the disk experiences transient rotation before recovering a stationary state or retaining a steady motion (see figure 2). Nevertheless, these situations are applicable only at a higher *e*, clearly distinguished by light-coloured symbols. When $e < 0.75$, the disk remains stationary or swims straight without any rotation. Besides, two types of periodic motions are depicted in the phase diagram: (1) a disk swings along a wavy trajectory (light-coloured squares); (2) a disk swims straight at an oscillating swimming speed (dark-coloured squares). The former and the latter are termed swinging and straight periodic motions, respectively.

4.2. *Spontaneous steady propulsion triggered by instability*

Upon gaining a general understanding of the phase diagram, we then explore the detailed swimming dynamics within each regime. We first focus on the transition from the stationary to steady swimming regime. The disk is stationary in the base state. As *Pe* exceeds $Pe_c^{(1)}$, an instability arises, and the disk sets into steady propulsion along its major axis. Here, we perform a LSA, as introduced in § 3, to identify quantitatively $Pe_c^{(1)}$ and its dependence on the disk shape. The $Pe_c^{(1)}$ value predicted by the LSA decreases monotonically with *e*, as depicted by the solid line in figure 3. Figure 4(*a*) depicts the concentration field $\hat{c}$ of the eigenmode at $Pe_c^{(1)} \approx 0.42$ for $e = 0.55$. We see that the symmetry of the base concentration field $\hat{c}$ is broken in the direction of the major axis at $Pe_c^{(1)}$. The fore–aft asymmetric concentration distribution induces a downward slip flow, as shown by the flow field $\hat{\boldsymbol{u}}$ of the eigenmode in figure 4(*b*), driving the steady motion of the disk along its major axis. In close proximity to $Pe_c^{(1)}$, the swimming speed U_{mg} is proportional to $\sqrt{Pe - Pe_c^{(1)}}$ (see figure 4*c*), implying that the instability occurs through a supercritical pitchfork bifurcation. This is parallel to the observation of Hu *et al.* (2019) and Li (2022).

We further probe the physical mechanism underlying the instability by adopting an approach resembling the energy budget analysis (Bendiksen 1985; Abubakar & Matar 2022). By taking an inner product, denoted by $(\cdot, \cdot)$, of (3.6) with $\hat{c}$ in the L^2 space, we arrive at

$$(\lambda\hat{c}, \hat{c}) + (\boldsymbol{u}_b \cdot \boldsymbol{\nabla}\hat{c}, \hat{c}) + (\hat{\boldsymbol{u}} \cdot \boldsymbol{\nabla}c_b, \hat{c}) = \frac{1}{Pe}(\Delta\hat{c}, \hat{c}). \tag{4.1}$$

Using integration by parts, the divergence-free condition in (3.5*a*,*b*), and the boundary conditions (3.7) and (3.8), we derive

$$(\boldsymbol{u}_b \cdot \boldsymbol{\nabla}\hat{c}, \hat{c}) = \tfrac{1}{2}(\boldsymbol{n} \cdot \boldsymbol{u}_b, \hat{c}^2)_{\Gamma_d} + \tfrac{1}{2}(\boldsymbol{n} \cdot \boldsymbol{u}_b, \hat{c}^2)_{\Gamma_o} = 0, \tag{4.2a}$$

$$(\hat{\boldsymbol{u}} \cdot \boldsymbol{\nabla}c_b, \hat{c}) = -(c_b, \hat{\boldsymbol{u}} \cdot \boldsymbol{\nabla}\hat{c}), \tag{4.2b}$$

$$\frac{1}{Pe}(\Delta\hat{c}, \hat{c}) = -\frac{1}{Pe}\|\boldsymbol{\nabla}\hat{c}\|^2, \tag{4.2c}$$

with $\|\cdot\|$ denoting the L^2-norm. By substituting (4.2) into (4.1), we obtain

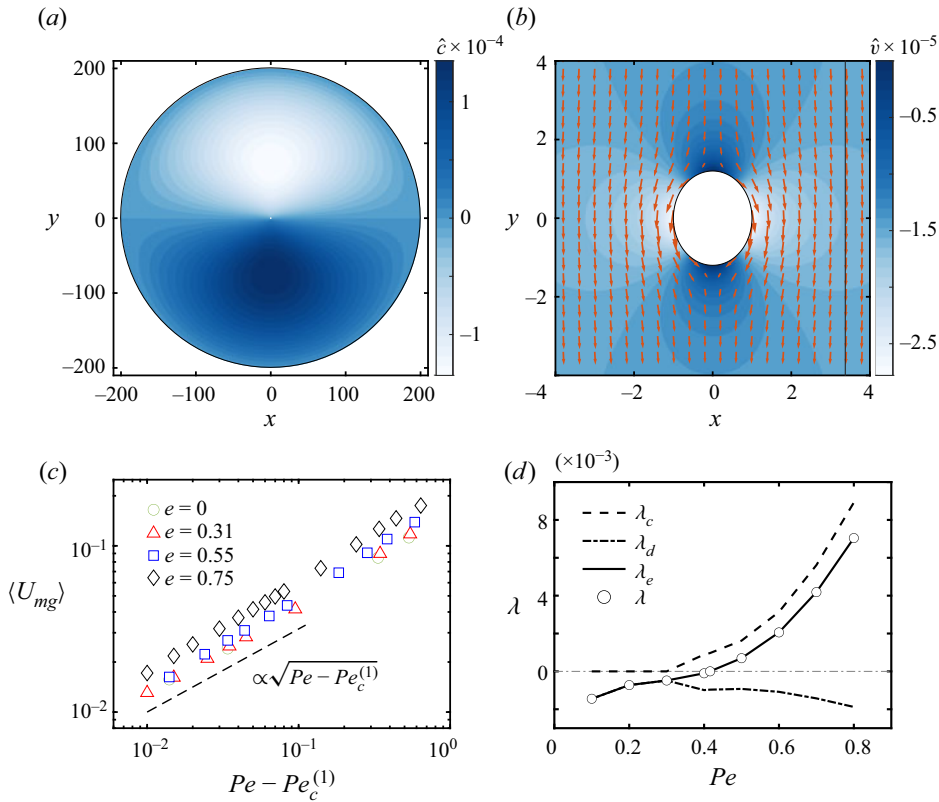$$\lambda_e = \lambda_c + \lambda_d, \tag{4.3}$$

Figure 4. Eigenmodes at the critical Péclet number $Pe_c^{(1)} \approx 0.42$ for an elliptical disk with $e = 0.55$. The eigenmode is characterized by (*a*) the perturbation concentration $\hat{c}$, and (*b*) the perturbation velocity $\hat{\boldsymbol{u}}$ (red arrows) and its y component $\hat{v}$ (colour map). (*c*) Dependence of time-averaged disk speed $\langle U_{mg} \rangle$ on $Pe - Pe_c^{(1)}$ at varying e. In the vicinity of $Pe_c^{(1)}$, $\langle U_{mg} \rangle$ is proportional to $\sqrt{Pe - Pe_c^{(1)}}$. (*d*) The Pe-dependent growth rate λ based on the LSA and $\lambda_e = \lambda_c + \lambda_d$ derived from the concentration perturbation equation (3.6). The latter comprises the contributions λ_c and λ_d from advection and diffusion, respectively.

with

$$\lambda_c = \frac{(c_b, \hat{\boldsymbol{u}} \cdot \boldsymbol{\nabla} \hat{c})}{(1, \hat{c}^2)}, \tag{4.4a}$$

$$\lambda_d = -\frac{\|\boldsymbol{\nabla} \hat{c}\|^2}{(Pe, \hat{c}^2)}. \tag{4.4b}$$

Here, the growth rate λ_e is introduced in (4.3) to be distinguished from λ obtained by the LSA. Also, λ_c and λ_d represent the contributions of advection and diffusion to λ_e, respectively. For a steady motion, the imaginary part of the growth rate vanishes, thus the growth rate has only its real part, e.g. $\lambda = \lambda_r$. Figure 4(*d*) shows that λ_e and λ lie on top of each other, giving us the confidence to analyse the dominant physical ingredient that drives the instability using (4.3). We infer naturally from (4.3) that λ_c is responsible for λ_e turning positive by realizing that λ_d is consistently negative, as confirmed by figure 4(*d*). Hence, as anticipated, advection drives the instability and diffusion dampens the perturbation, and the balance between them dominates the phoretic dynamics of the
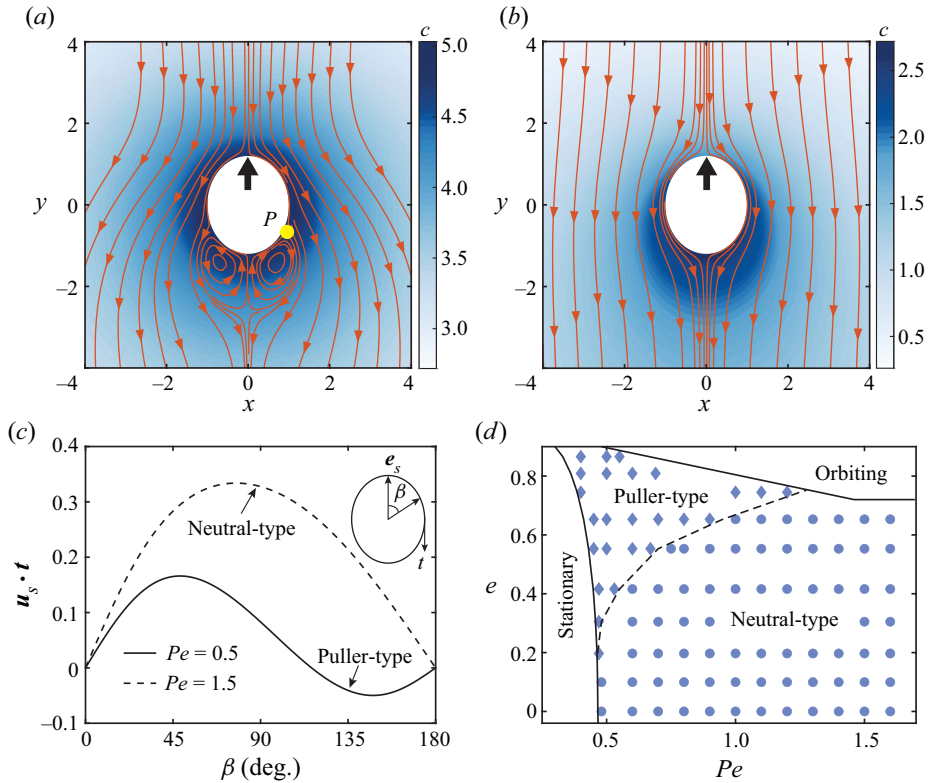
Figure 5. (*a*) A puller-type steady swimmer at $Pe = 0.5$ transitions to (*b*) a neutral-type counterpart at $Pe = 1.5$, where the eccentricity e is 0.55. The flow fields are shown in the frame co-moving with the disk. Black arrows denote swimming direction. The colour maps indicate the distribution of c. The stagnation point P coincides with the peak of c at the disk surface. (*c*) Polar velocity magnitude $\boldsymbol{u}_s \cdot \boldsymbol{t}$ at the disk surface, following the definition in Downton & Stark (2009). Here, β is the polar angle with respect to the disk orientation $\boldsymbol{e}_s$, with $\boldsymbol{t}$ the corresponding unit tangent vector. (*d*) Pe–e phase diagram shows puller-type and neutral-type steady swimmers demarcated by the dashed line. Solid lines separate regimes identified in figure 3.

elliptical disk: at small Pe, diffusion dominates, and its homogenizing effect maintains a fore–aft symmetric solute distribution. As Pe grows beyond $Pe_c^{(1)}$, advection suppresses diffusion and amplifies the asymmetric solute disturbance. The slip flows triggered by the asymmetric concentration distribution drive the disk to swim spontaneously.

Next, we analyse the steady propulsion of the autophoretic disk. We show in figures 5(*a,c*) that the elliptical disk with $e = 0.55$ swims as a puller, attracting the fluid from its front and rear at $Pe = 0.5$. In contrast, it becomes a neutral-type swimmer at $Pe = 1.5$, as indicated in figures 5(*b,c*). In retrospect, Suda *et al.* (2021) reported an analogous transition from a puller swimming straight into a pusher-type swimmer executing unsteady curvilinear motion when Pe increases. In that case, the droplet motion is triggered by the concentration gradient caused by a point source of surfactant at the surface. Besides, Li (2022) observes that an active drop transits from a steady pusher to a mixed pusher–puller propelling unsteadily as Pe grows. In the case of these droplet swimmers, the switching of their disturbance flow occurs as they go from steady to unsteady motion. Morozov & Michelin (2019*a*) describes a Pe-dependent neutral-to-pusher transition for a 3-D axisymmetric droplet impelling steadily. Notably, this transition occurs without a shift
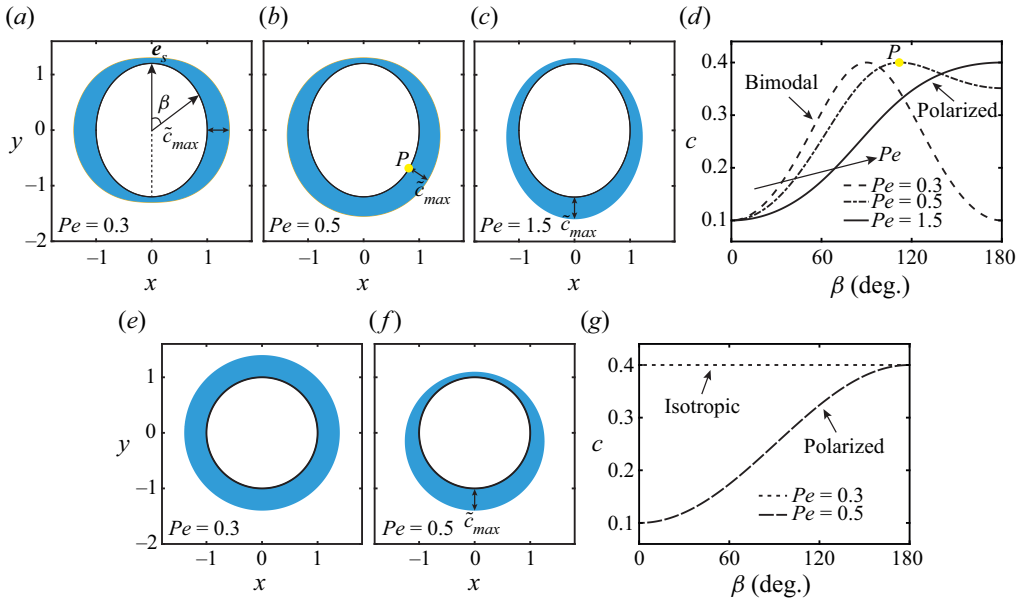
974 A57-12

Figure 6. Normalized concentration at the surface of a disk swimming steadily: (a–c) for an elliptical disk with $e = 0.55$ at $Pe = 0.3$, 0.5 and 1.5, respectively; (e,f) for a circular disk at $Pe = 0.3$ and 0.5, respectively. Here, c_{max} denotes the peak concentration at the disk surface. The stagnation point P coincides with the location of $\tilde{c}_{max}$ at $Pe = 0.5$. (d) Transition from a bimodal to a polarized concentration distribution at the surface of an elliptical disk by increasing Pe. (g) Similar to (d), but for a circular disk with a transition from an isotropic solute distribution.

in the droplet's swimming pattern, resembling that exhibited by the disk swimmer here. We examine further the flow field in the frame co-moving with the disk throughout the whole steady swimming regime, and summarize these results in a phase diagram in figure 5(d). It is found that a circular ($e = 0$) or nearly circular disk can be only a neutral swimmer, and the puller-to-neutral transition emerges as $e \geq 0.20$. The critical Péclet number Pe_t signifying this transition depends monotonically on e, as indicated by the dashed line. When $e > 0.65$, the transition disappears and the disk swims solely as a puller. In fact, this peculiar transformation can be understood by examining the solute distribution at the disk surface, as discussed below. For visualization purposes, we normalize the concentration via $\tilde{c} = 0.3(c_{max} - c)/(c_{max} - c_{min})$, where c_{max} and c_{min} denote the maximum and minimum concentrations at the disk surface, respectively.

We demonstrate in figures 6(a,d) the bimodal distribution of normalized concentration caused by the curvature variation of the disk surface in the base state ($Pe = 0.3$). The maximum normalized concentration $\tilde{c}_{max}$ is located at the left vertex of the minor axis corresponding to $\beta = 90°$, where β denotes the polar angle with respect to e_s. Here, we consider only the left half of the disk ($\beta \in [0, 180°]$) for its symmetry. At $Pe = 0.5$, the base state loses stability and solutes are advected toward the disk's rear ($\beta = 180°$). Correspondingly, the position of c_{max} migrates rearwards from $\beta = 90°$ to the stagnation point P, as depicted in figure 6(b). Considering that the slip velocity $u_s = \nabla_s c$ is directed from low to high concentration at the disk surface, the fluid is attracted from the front and rear of the elliptical disk to the stagnation position P, forming a puller-type swimmer (see figure 5a). As Pe increases to 1.5, the enhanced convective transport of solutes causes the shift from a bimodal to a polarized concentration profile with the peak concentration located at $\beta = 180°$ (see figure 6c). Correspondingly, the slip flow induced
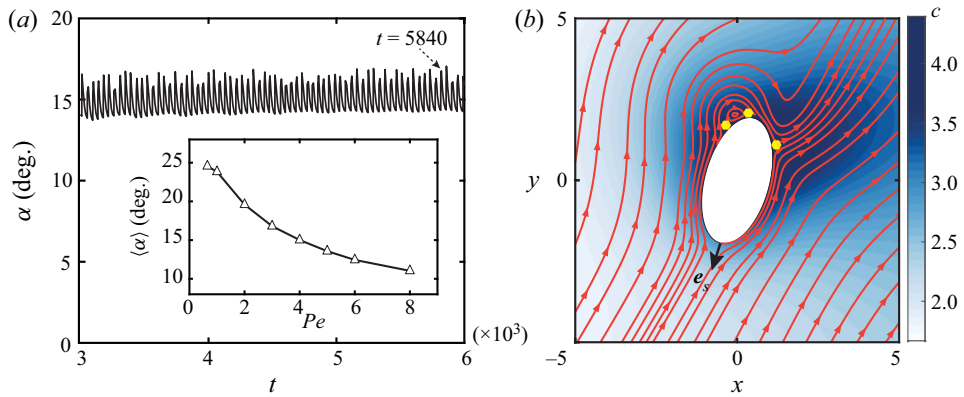
Figure 7. (*a*) Time evolution of the angle α between the translational velocity U and the disk orientation e_s as the elliptical disk with $e = 0.87$ approximately follows a circular trajectory for $Pe = 4$. The inset shows the monotonic decrease of the time-averaged α with Pe. (*b*) Solute distribution and streamlines at the instant $t = 5840$ marked in (*a*). Three hexagons denote the stagnation points at the rear of the disk.

by the concentration gradient is driven from the front to the rear of the disk (see figure 6*b*), generating a prototypical neutral-type swimmer. We comment that as an elliptical disk swims steadily, a bimodal concentration profile at its surface yields a puller-type swimmer, while a polarized one leads to a neutral-type counterpart. Different from the elliptical disk, a circular disk has an isotropic base distribution of the solute ($Pe = 0.3$), as shown in figures 6(*e,g*). For an unstable base state at $Pe = 1.5$, solutes are advected rearwards along the disk surface, leading to the direct transition from an isotropic to a polarized concentration profile. Hence the circular disk behaves as a neutral swimmer solely.

4.3. *Chiral symmetry-breaking orbiting motion*

Having observed the puller–neutral transition in the steady swimming regime, we direct our focus onto the chiral symmetry-breaking orbiting motion of the elliptical disk. Here, the disk swims approximately along a circular trajectory (see figure 2*b*) with rotational velocity Ω. The time evolution of Ω resembles that of α in figure 7(*a*) oscillating around a constant value: the constant value determines a globally circular trajectory, and the oscillations contribute to a locally undulatory trajectory. We find that the translational velocity U (green arrow in figure 2*b*) deviates from e_s (red arrow) by an angle α oscillating slightly around $15°$ for $Pe = 4$. In fact, the misalignment of U and e_s can be rationalized by examining the solute distribution $c(x, y)$ around the disk. Figure 7(*b*) illustrates $c(x, y)$ and streamlines at a specific moment $t = 5840$. The left–right asymmetry of the solute distribution about e_s gives rise to the asymmetric slip velocity, as reflected by the streamlines, hence causing diverging directions of U and e_s. Besides, we notice that three stagnation points near the rear of the disk in figure 7(*b*) migrate gradually towards the rear with increasing Pe in the orbiting regime (not shown here). Accordingly, the time-averaged $\langle\alpha\rangle = \int_0^T \alpha \, dt/T$ within a time window T decreases monotonically with Pe, as shown in the inset of figure 7(*a*). Intuitively, we infer that U is aligned with e_s ($\alpha = 0$) as the three stagnation points coincide exactly at the rear of the disk, and indeed they do as Pe grows beyond 14 where the disk executes a steady motion, e.g. $Pe = 25$ (streamlines and concentration distribution are analogous to figure 5*b*).
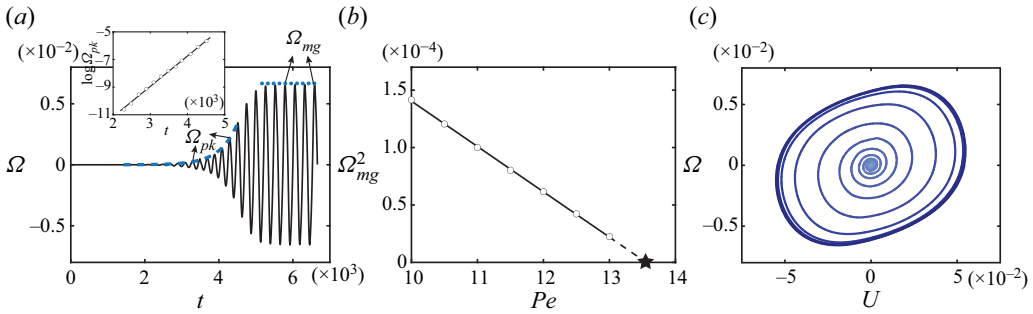
974 A57-14

Figure 8. (*a*) Time evolution of the rotational velocity Ω of an elliptical disk with $e = 0.87$ at $Pe = 12.5$. The dashed line denotes certain local peaks Ω_{pk} of Ω, and the inset shows the linear dependence of $\log \Omega_{pk}$ on t. (*b*) Linear variation of Ω_{mg}^2 in Pe near the critical $Pe \approx 13.5$ (star), where Ω_{mg} denotes the constant amplitude of Ω at $t > 5400$, as depicted by the dotted line in (*a*). The periodic motion recovers to steady propulsion as Pe grows beyond the critical value. (*c*) Phase portrait in the Ω–U plane, with the colour of the unstable spiral coded by t.

The orbiting regime is characterized by the continuous rotation of an elliptical disk, which loses its chiral symmetry spontaneously. Conversely, a circular disk maintains this symmetry irrespective of the *Pe* value. In particular, for $Pe \in [9, 13]$, despite the asymmetric solute distribution and streamlines resembling those in figure 7(*b*) occasionally, the circular disk executes only a meandering motion (Hu *et al.* 2019) without rotation. Ideally, a secondary stability analysis similar to the one performed above will help us to understand the mechanism for the shape-induced chiral symmetry breaking. This task is, however, technically challenging, and will be pursued in the future.

Notably, experiments on active droplets in a Hele-Shaw cell showed that the droplet preferred to avoid the concentration trail emitted by itself at earlier times, termed a self-avoiding walk phenomenon (Hokmabad *et al.* 2021). The elliptical disk here does not avoid similarly but instead repeats its previous trajectory, as shown in figure 2(*b*). The difference can be rationalized by a scaling analysis. We estimate that the time $\bar{t}_d$ required for the concentration to decay to zero is of the order of $\bar{b}^2/\bar{D}$. The disk moves with speed $U_{mg}\bar{\mathcal{V}}$, hence the travelling time $\bar{t}_p$ taken to execute a circular trajectory of perimeter $\bar{L}_p$ is $\bar{L}_p/(U_{mg}\bar{\mathcal{V}})$, approximately. Recalling the definitions of $\bar{\mathcal{V}}$ and *Pe* in §2, we rewrite $\bar{t}_p$ as $\bar{L}_p\bar{b}/(U_{mg}\,Pe\,\bar{D})$. The ratio between these two time scales is

$$\frac{\bar{t}_p}{\bar{t}_d} = \frac{\bar{L}_p/\bar{b}}{U_{mg}\,Pe}. \tag{4.5}$$

At a specific *Pe*, e.g. $Pe = 4$, in the orbiting regime, $\bar{t}_p/\bar{t}_d \approx 87.2 \gg 1$. This substantial ratio indicates that the disk swimmer can barely sense and thus avoid its own rapidly decaying chemical trace. In contrast, for a sufficiently larger *Pe*, we may observe the self-avoidance due to the significantly reduced travel time t_p (Hokmabad *et al.* 2021; Hu *et al.* 2022).

4.4. *Periodic swinging*

Typically, the orbiting motion transitions to periodic swinging (refer to figure 2*c*) as *Pe* increases, which will be analysed below. Figure 8(*a*) illustrates that the time-evolving rotational velocity Ω of the disk with $e = 0.87$ at $Pe = 12.5$ is characterized by two phases.

First, Ω grows rapidly due to self-oscillation, and the dashed line connecting local peaks Ω_{pk} of Ω indicates an exponential growth of Ω in time. This trend is confirmed by the linear relationship between $\log \Omega_{pk}$ and t shown in the inset of figure 8(*a*). Second, Ω saturates nonlinearly to a periodic state with a constant amplitude Ω_{mg}. The sinusoidal-like variation of Ω leads to a wave-like trajectory. We plot Ω_{mg}^2 as a function of *Pe* near the critical $Pe \approx 13.5$ (star) in figure 8(*b*). The linear dependence of Ω_{mg}^2 on *Pe* implies that the steady motion loses stability through a Hopf bifurcation. The critical *Pe* signifies the boundary between the periodic swinging and steady motion. We further present in figure 8(*c*) the phase portrait in the Ω–*U* plane, where the unstable spiral at the origin grows continuously to an elliptical stable limit circle, indicating the supercritical nature of the Hopf bifurcation. Notably, when $e < 0.87$, we observe a transition from steady to periodic swinging with increasing *Pe*, e.g. $e = 0.81$ (see figure 3). The Hopf bifurcation still holds for the onset of instability that triggers this transition.

4.5. *Chaotic swimming dynamics*

Finally, we analyse the chaotic motion of elliptical disks by examining their mean square displacement (MSD) and the velocity autocorrelation function (VAF). We calculate the MSD(τ) of a disk (Michalet 2010) that depends on a time lag τ by

$$\mathrm{MSD}(\tau) = \frac{1}{T-\tau} \int_0^{T-\tau} [\boldsymbol{r}(t+\tau) - \boldsymbol{r}(t)]^2 \, \mathrm{d}t, \tag{4.6}$$

where $\boldsymbol{r}(t)$ denotes the time-dependent displacement of a disk relative to its original position. Clearly, combining a large time period T and $\tau \ll T$ can improve the statistical confidence. We calculate VAF using

$$\mathrm{VAF}(t) = \frac{1}{T} \int_0^T \frac{\boldsymbol{U}(t) \cdot \boldsymbol{U}(t+\Delta t)}{|\boldsymbol{U}(t)| \, |\boldsymbol{U}(t+\Delta t)|} \, \mathrm{d}t, \tag{4.7}$$

where a sufficiently large T is used to attain statistical invariance (Chen *et al.* 2021).

We examine how the eccentricity e of a disk affects its chaotic motion. First, we determine the shape-dependent $Pe_c^{(2)}(e)$ when chaos emerges. Then we investigate the chaotic dynamics at $Pe(e) = Pe_c^{(2)}(e) + 10$ above that threshold by a fixed offset, namely 10 here. The corresponding MSD and VAF are depicted in figure 9(*a*). At early times, despite the diversity in the disk shape, they all swim persistently, resulting in the quadratically growing MSD in τ. At long times, the disk shape considerably affects its phoretic movement, leading to a transition from a random-walking circular disk to a ballistically swimming elliptical counterpart. For the former, we reproduce perfectly its random walk behaviour as reported by Hu *et al.* (2019, 2022) and Lin, Hu & Misbah (2020), which features the linear scaling MSD $\propto \tau$ and the decorrelation in velocity U due to the rapidly changing swimming direction (see the inset). As the eccentricity e increases to 0.1, MSD $\propto \tau^{1.5}$, reminiscent of the self-avoidance walk identified experimentally (Hokmabad *et al.* 2021). We wonder whether this growth scaling, $\propto \tau^{1.5}$, results from the self-avoidance walk. By utilizing the scaling analysis mentioned above, we compare the decay time of the chemical $\bar{t}_d$ and the travelling time $\bar{t}_p$ of the disk, and find that $\bar{t}_p/\bar{t}_d \approx 40.8 \gg 1$ (see (4.5)), precluding self-avoidance here. At $e = 0.87$, the MSD's quadratic growth over lag time implies that the elliptical disk approximately executes the ballistic motion, as confirmed by the trajectory shown in figure 2(*e*). Accordingly, the VAF is almost constant in time, indicating a correlation in velocity U. It is worth noting that
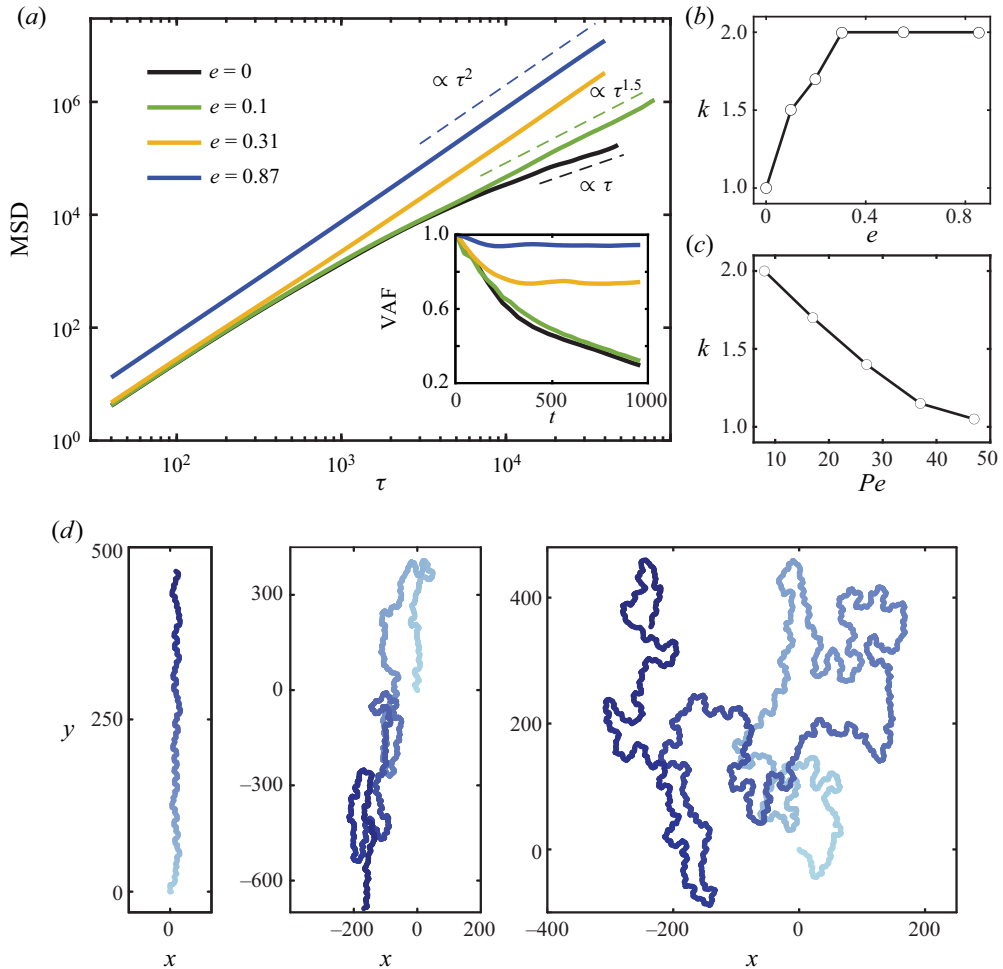
Figure 9. (*a*) Mean square displacement (MSD) and velocity autocorrelation function (VAF) for disks with different shapes at $Pe_c^{(2)} + 10$, where $Pe_c^{(2)}$ is the shape-dependent critical Péclet number corresponding to the onset of chaos. (*b*) The exponent k of the power-law scaling MSD $\propto \tau^k$ versus e. (*c*) Monotonic dependence of k on Pe for the disk of $e = 0.2$. (*d*) Chaotic trajectories (colour-coded by t) followed by an elliptical disk of $e = 0.2$ at $Pe = 8$, 27 and 47, respectively.

Hu *et al.* (2022) and Morozov & Michelin (2019*a*) also found the quadratic variations of MSD for the chaotic swimming of a phoretic particle and an active droplet, respectively, under the axisymmetric assumption.

By probing further in figure 9(*b*) the exponent k of power-law scaling MSD $\propto \tau^k$ at varying e, we notice that the normal diffusion ($k = 1$) transitions to superdiffusion ($k > 1$) as e increases. This observation demonstrates that the shape of a disk can significantly affect its diffusion behaviour. In addition, we explore the effect of Pe on the chaotic motion of an elliptical disk at long times, as depicted in figure 9(*c*). In contrast to the eccentricity e, k decreases monotonically with Pe, implying the transition from superdiffusion to normal diffusion. Accordingly, the elliptical disk undergoes a ballistic motion near $Pe_c^{(2)}$ and swims randomly at a larger Pe, e.g. $Pe = 47$ (see figure 9*d*). An analogous dependence of k on Pe for the chaotic motion of an axisymmetric spherical particle was also reported by

Kailasham & Khair (2022). Note that the system exhibits ballistic evolution (MSD $\propto \tau^2$) at short times regardless of *Pe*.

5. Conclusions and discussions

In this work, we investigate numerically and theoretically the swimming dynamics of an elliptical disk releasing solutes uniformly in the creeping flow regime. The disk with an eccentricity $e < 0.75$ mimics a circular counterpart: it shows stationary, steady, periodic and chaotic behaviours, dependent on *Pe*. When $e > 0.75$, the disk attains an orbiting motion via an instability spontaneously breaking the chiral symmetry.

By performing an LSA, we predict theoretically the critical Péclet number $Pe_c^{(1)}$ above which a stationary disk becomes a steady swimmer spontaneously triggered by instability. Besides the LSA, we calculate the perturbation growth rate via a method akin to energy budget analysis. The results agree with the LSA predictions, and two contributing components of the growth rate showcase the competing roles of advection and diffusion.

We observe that the transition from a puller-type to a neutral-type steady disk swimmer is induced by a stronger rearward advection of solute due to growing *Pe*. Accordingly, a bimodal concentration profile corresponding to a puller-type swimmer becomes a polarized profile leading to a neutral-type swimmer. The orbiting disk repeatedly swims along a circular trajectory while simultaneously rotating.

Two distinct types of periodic motion are identified: swinging and straight. The former develops from a steady motion through a supercritical Hopf bifurcation, and features a wave-like trajectory. The latter is characterized by a rectilinear motion with an oscillating swimming speed. Finally, the effects of the disk shape and *Pe* on the chaotic motion are examined. We uncover a shift from normal diffusion to superdiffusion with growing eccentricity *e*: the former and latter correspond to a random-walking circular disk and a ballistically swimming elliptical counterpart, respectively. The influence of *Pe* on the disk's diffusion behaviour stands in contrast to that of *e*.

It is worth mentioning that the prolate Janus droplet, as reported experimentally (Meredith *et al.* 2022), propels along its major axis resembling the behaviour of our elliptical disk in the steady swimming regime. Nevertheless, the swimming orientation of the Janus droplet is determined by the inherent asymmetry of surface activity along its major axis, rather than by the instability-induced symmetry breaking. Additionally, we would like to emphasize that both the elliptical camphor disk (Kitahata *et al.* 2013) and the prolate composite droplet (Hokmabad *et al.* 2019) in experiments demonstrated self-propulsion along their minor axes, rather than the major axis that we observe. The differences may result from the failure of 2-D simulations to capture the complex 3-D physico-chemical hydrodynamics present in experiments. Specifically, a swimming camphor disk is driven by Marangoni flow at the air–liquid interface and the resulting 3-D subsurface flow, while the prolate droplet self-propels within a Hele-Shaw cell. We are planning 3-D studies to address these discrepancies.
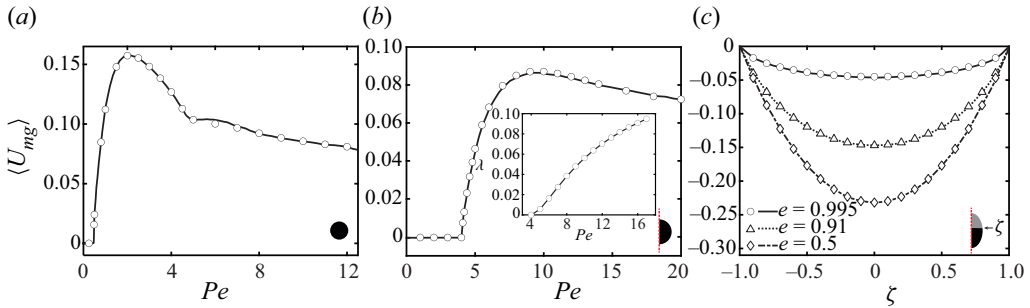
Figure 10. Validation of our numerical implementation against published works. The numerical and published data are represented by markers and lines, respectively. (*a*) Swimming speed of an isotropic autophoretic disk in a circular domain of radius $R = 200$ for varying *Pe*, benchmarked by Hu *et al.* (2019). Note that the time-averaged swimming speed $\langle U_{mg} \rangle = \int_0^T U_{mg} \, dt$ within a time period T recovers U_{mg} for steady propulsion. (*b*) Swimming speed of an autophoretic spherical particle versus *Pe* computed in an axisymmetric configuration, in comparison to Michelin *et al.* (2013); the inset shows the growth rate λ of the unstable eigenmode versus *Pe*. (*c*) Swimming velocity of a spheroidal Janus particle as a function of ζ, validated against Popescu *et al.* (2010). Here, ζ denotes the height of the border dividing the particle into active and inert (marked in grey) compartments, with $\zeta = 0$ corresponding to the particle centre. The eccentricity e of the spheroid recovers to zero for a spherical particle.

Declaration of interests. The authors report no conflict of interest.

Author ORCIDs.

ⓘ Guangpu Zhu https://orcid.org/0000-0002-7721-0685;

ⓘ Lailai Zhu https://orcid.org/0000-0002-3443-0709.

Appendix A. Validation of numerical implementations

We show the validation of our COMSOL implementations for the numerical simulation (2.3*a*,*b*)–(2.8) and stability analysis (3.5*a*,*b*)–(3.9). First, we study the inertialess self-propulsion of an isotropic autophoretic disk in a circular domain of radius $R = 200$. This set-up has been investigated by Hu *et al.* (2019), combining a stability analysis and simulations based on a spectral method. The disk transits to a steady swimmer from its stationary state at the first threshold $Pe \approx 0.466$. Increasing *Pe*, the swimmer becomes unstable at the second critical condition $Pe \approx 4.65$, moving in a meandering manner. Our numerical data shown in figure 10(*a*) recover exactly the reported *Pe*-dependent swimming speed and two critical *Pe* values. Besides the 2-D case, we examine the spontaneous motion of an axisymmetric isotropic particle in an unbounded domain. In this case, instability occurs at $Pe = 4$, as predicted by Michelin *et al.* (2013). Our data on swimming speed agree well with the numerical results therein, as depicted in figure 10(*b*). Also, its inset shows that the present LSA recovers the threshold $Pe = 4$ and the eigenvalues depending on *Pe*. As a side product, we probe the effect of inertia *Re* on this scenario. The inertial effect systematically enhances the swimming speed, becoming pronounced when $Re > 1$ (see figure 11*a*). The inertia-induced relative enhancement of the swimming speed ε in figure 11(*b*) is observed to scale linearly with *Re* in this weak inertia regime, which deserves further theoretical underpinning.

Finally, we examine the ability of our implementation in handling non-spherical phoretic swimmers. We focus on a spheroidal Janus colloid consisting of active and inert compartments. Its propulsion depends on its eccentricity e and ζ, where ζ denotes the height of the border separating the two compartments. The obtained swimming speed
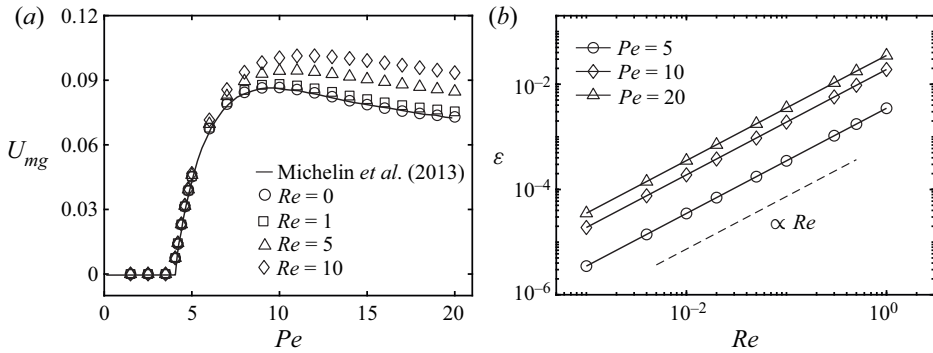
Figure 11. (*a*) Swimming speed U_{mg} of an isotropic phoretic particle versus Pe when Re varies, which is calculated in an axisymmetric set-up. Our numerical data are compared with those of Michelin *et al.* (2013) at $Re = 0$. (*b*) Inertia enhances the swimming speed, characterized by the linear relation between the relative enhancement $\varepsilon = [U_{mg}(Re, Pe) - U_{mg}(Re = 0, Pe)]/U_{mg}(Re = 0, Pe)$ and Re.
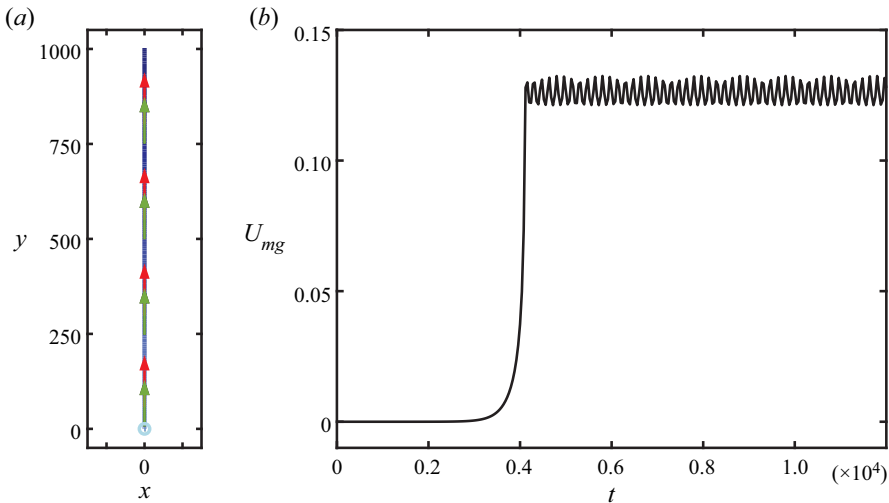

Figure 12. Straight periodic motion of an elliptical disk with $e = 0.87$ at $Pe = 33$. (*a*) Straight trajectory colour-coded by time t. The swimming direction $\boldsymbol{e}_s$ (red arrow) coincides with the translational velocity $\boldsymbol{U}$ (green arrow). (*b*) Time evolution of the swimming speed U_{mg}.

agrees well with the reference solutions over a wide range of e and ζ (Popescu *et al.* 2010), as shown in figure 10(*c*).

Appendix B. Periodic motion of an elliptical phoretic disk

We identify two types of periodic motion: the first showcases a wave-like trajectory caused by the periodic rotation of the elliptical disk (see figure 2*g*); the second corresponds to unidirectional rectilinear motion with a time-periodic swimming speed, as shown in figure 12.
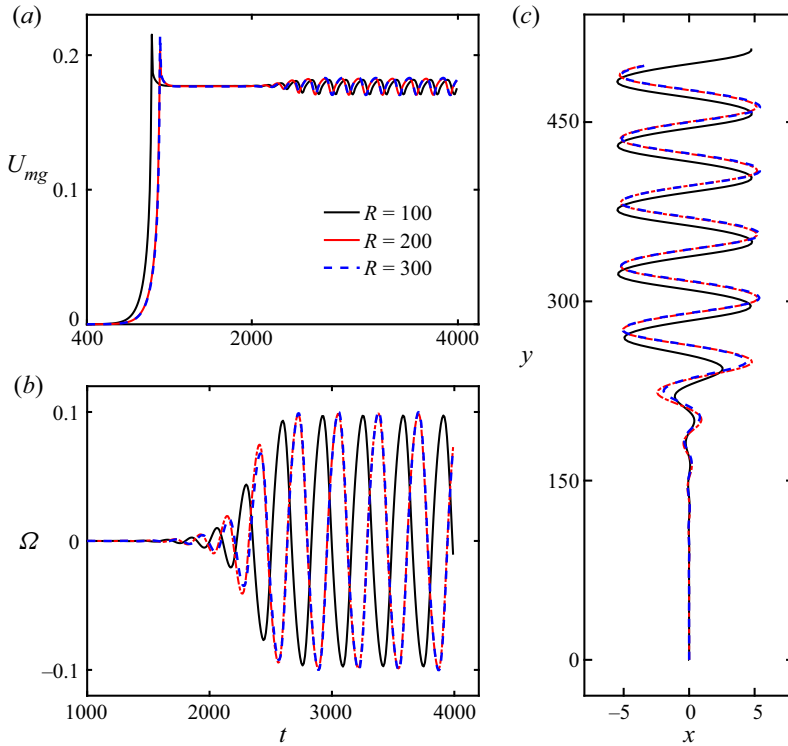
974 A57-20

Figure 13. (*a*) Swimming speeds, (*b*) rotational velocities, and (*c*) trajectories of an elliptical disk with $e = 0.87$ and $Pe = 11$ at varying R. Results at $R = 200$ and $R = 300$ lie almost on top of each other.

Appendix C. Dependency of swimming dynamics on the domain size R

In figure 13, we show the dependency of a disk's swimming dynamics on the domain size R. The results obtained at $R = 200$ agree perfectly with those at $R = 300$, suggesting that the selected size $R = 200$ should be sufficiently large.

REFERENCES

ABUBAKAR, H.A. & MATAR, O.K. 2022 Linear stability analysis of Taylor bubble motion in downward flowing liquids in vertical tubes. *J. Fluid Mech.* **941**, A2.

AHMED, D., BAASCH, T., JANG, B., PANE, S., DUAL, J. & NELSON, B.J. 2016 Artificial swimmers propelled by acoustically activated flagella. *Nano Lett.* **16** (8), 4968–4974.

ANDERSON, J.L. 1989 Colloid transport by interfacial forces. *Annu. Rev. Fluid Mech.* **21** (1), 61–99.

BAN, T., SUGIYAMA, M., NAGATSU, Y. & TOKUYAMA, H. 2018 Motion-based detection of lanthanides(III) using self-propelled droplets. *J. Phys. Chem.* B **122** (46), 10647–10651.

BENDIKSEN, K.H. 1985 On the motion of long bubbles in vertical tubes. *Intl J. Multiphase Flow* **11** (6), 797–812.

DE BLOIS, C., REYSSAT, M., MICHELIN, S. & DAUCHOT, O. 2019 Flow field around a confined active droplet. *Phys. Rev. Fluids* **4** (5), 054001.

BONIFACE, D., COTTIN-BIZONNE, C., DETCHEVERRY, F. & YBERT, C. 2021 Role of Marangoni forces in the velocity of symmetric interfacial swimmers. *Phys. Rev. Fluids* **6** (10), 104006.

BRADY, J.F. 2011 Particle motion driven by solute gradients with application to autonomous motion: continuum and colloidal perspectives. *J. Fluid Mech.* **667**, 216–259.

CAMPBELL, A.I., EBBENS, S.J., ILLIEN, P. & GOLESTANIAN, R. 2019 Experimental observation of flow fields around active Janus spheres. *Nat. Commun.* **10** (1), 1–8.

CHEN, Y., CHONG, K.L., LIU, L., VERZICCO, R. & LOHSE, D. 2021 Instabilities driven by diffusiophoretic flow on catalytic surfaces. *J. Fluid Mech.* **919**, A10.

DADDI-MOUSSA-IDER, A., VILFAN, A. & GOLESTANIAN, R. 2022 Diffusiophoretic propulsion of an isotropic active colloidal particle near a finite-sized disk embedded in a planar fluid–fluid interface. *J. Fluid Mech.* **940**, A12.

DATT, C., NATALE, G., HATZIKIRIAKOS, S.G. & ELFRING, G.J. 2017 An active particle in a complex fluid. *J. Fluid Mech.* **823**, 675–688.

DESAI, N. & MICHELIN, S. 2021 Instability and self-propulsion of active droplets along a wall. *Phys. Rev. Fluids* **6** (11), 114103.

DEY, R., BUNESS, C.M., HOKMABAD, B.V., JIN, C. & MAASS, C.C. 2022 Oscillatory rheotaxis of artificial swimmers in microchannels. *Nat. Commun.* **13** (1), 1–10.

DOWNTON, M.T. & STARK, H. 2009 Simulation of a model microswimmer. *J. Phys.: Condens. Mater* **21** (20), 204101.

DREYFUS, R., BAUDRY, J., ROPER, M.L., FERMIGIER, M., STONE, H.A. & BIBETTE, J. 2005 Microscopic artificial swimmers. *Nature* **437** (7060), 862–865.

DUAN, W., WANG, W., DAS, S., YADAV, V., MALLOUK, T.E. & SEN, A. 2015 Synthetic nano- and micromachines in analytical chemistry: sensing, migration, capture, delivery, and separation. *Annu. Rev. Anal. Chem.* **8**, 311–333.

DWIVEDI, P., SHRIVASTAVA, A., PILLAI, D. & MANGAL, R. 2021 Rheotaxis of active droplets. *Phys. Fluids* **33** (8), 082108.

EBRAHIMI, N., *et al.* 2021 Magnetic actuation methods in bio/soft robotics. *Adv. Funct. Mater.* **31** (11), 2005137.

GHOSH, A. & FISCHER, P. 2009 Controlled propulsion of artificial magnetic nanostructured propellers. *Nano Lett.* **9** (6), 2243–2245.

GOLESTANIAN, R., LIVERPOOL, T.B. & AJDARI, A. 2007 Designing phoretic micro- and nano-swimmers. *New J. Phys.* **9** (5), 126.

HOKMABAD, B.V., AGUDO-CANALEJO, J., SAHA, S., GOLESTANIAN, R. & MAASS, C.C. 2022 Chemotactic self-caging in active emulsions. *Proc. Natl Acad. Sci. USA* **119** (24), e2122269119.

HOKMABAD, B.V., BALDWIN, K.A., KRÜGER, C., BAHR, C. & MAASS, C.C. 2019 Topological stabilization and dynamics of self-propelling nematic shells. *Phys. Rev. Lett.* **123** (17), 178003.

HOKMABAD, B.V., DEY, R., JALAAL, M., MOHANTY, D., ALMUKAMBETOVA, M., BALDWIN, K.A., LOHSE, D. & MAASS, C.C. 2021 Emergence of bimodal motility in active droplets. *Phys. Rev.* X **11** (1), 011043.

HU, W.-F., LIN, T.-S., RAFAI, S. & MISBAH, C. 2019 Chaotic swimming of phoretic particles. *Phys. Rev. Lett.* **123** (23), 238004.

HU, W.-F., LIN, T.-S., RAFAI, S. & MISBAH, C. 2022 Spontaneous locomotion of phoretic particles in three dimensions. *Phys. Rev. Fluids* **7** (3), 034003.

IIDA, K., KITAHATA, H. & NAGAYAMA, M. 2014 Theoretical study on the translation and rotation of an elliptic camphor particle. *Phys.* D **272**, 39–50.

IZRI, Z., VAN DER LINDEN, M.N., MICHELIN, S. & DAUCHOT, O. 2014 Self-propulsion of pure water droplets by spontaneous Marangoni-stress-driven motion. *Phys. Rev. Lett.* **113** (24), 248302.

JIN, C., HOKMABAD, B.V., BALDWIN, K.A. & MAASS, C.C. 2018 Chemotactic droplet swimmers in complex geometries. *J. Phys.: Condens. Matter* **30** (5), 054003.

JIN, C., KRÜGER, C. & MAASS, C.C. 2017 Chemotaxis and autochemotaxis of self-propelling droplet swimmers. *Proc. Natl Acad. Sci. USA* **114** (20), 5089–5094.

JOH, H. & FAN, D.E. 2021 Materials and schemes of multimodal reconfigurable micro/nanomachines and robots: review and perspective. *Adv. Mater.* **33** (39), 2101965.

KAGAN, D., LAOCHAROENSUK, R., ZIMMERMAN, M., CLAWSON, C., BALASUBRAMANIAN, S., KANG, D., BISHOP, D., SATTAYASAMITSATHIT, S., ZHANG, L. & WANG, J. 2010 Rapid delivery of drug carriers propelled and navigated by catalytic nanoshuttles. *Small* **6** (23), 2741–2747.

KAILASHAM, R. & KHAIR, A.S. 2022 Dynamics of forced and unforced autophoretic particles. *J. Fluid Mech.* **948**, A41.

KAILASHAM, R. & KHAIR, A.S. 2023 Non-Brownian diffusion and chaotic rheology of autophoretic disks. *Phys. Rev.* E **107** (4), 044609.

KASUO, Y., KITAHATA, H., KOYANO, Y., TAKINOUE, M., ASAKURA, K. & BANNO, T. 2019 Start of micrometer-sized oil droplet motion through generation of surfactants. *Langmuir* **35** (41), 13351–13355.

KITAHATA, H., IIDA, K. & NAGAYAMA, M. 2013 Spontaneous motion of an elliptic camphor particle. *Phys. Rev.* E **87** (1), 010901.

KOHL, R., CORONA, E., CHERUVU, V. & VEERAPANENI, S. 2023 Fast and accurate solvers for simulating Janus particle suspensions in Stokes flow. *Adv. Comput. Maths* **49** (4), 45.

KOLEOSO, M., FENG, X., XUE, Y., LI, Q., MUNSHI, T. & CHEN, X. 2020 Micro/nanoscale magnetic robots for biomedical applications. *Mater. Today Bio* **8**, 100085.

KRÜGER, C., KLÖS, G., BAHR, C. & MAASS, C.C. 2016 Curling liquid crystal microswimmers: a cascade of spontaneous symmetry breaking. *Phys. Rev. Lett.* **117** (4), 048003.

LATTUADA, M. & HATTON, T.A. 2011 Synthesis, properties and applications of Janus nanoparticles. *Nano Today* **6** (3), 286–308.

LAUGA, E. & POWERS, T.R. 2009 The hydrodynamics of swimming microorganisms. *Rep. Prog. Phys.* **72** (9), 096601.

LI, G. 2022 Swimming dynamics of a self-propelled droplet. *J. Fluid Mech.* **934**, A20.

LI, M., PAL, A., AGHAKHANI, A., PENA-FRANCESCH, A. & SITTI, M. 2022 Soft actuators for real-world applications. *Nat. Rev. Mater.* **7** (3), 235–249.

LIN, T.-S., HU, W.-F. & MISBAH, C. 2020 A direct Poisson solver in spherical geometry with an application to diffusiophoretic problems. *J. Comput. Phys.* **409**, 109362.

LIPPERA, K., BENZAQUEN, M. & MICHELIN, S. 2020a Bouncing, chasing, or pausing: asymmetric collisions of active droplets. *Phys. Rev. Fluids* **5** (3), 032201.

LIPPERA, K., MOROZOV, M., BENZAQUEN, M. & MICHELIN, S. 2020b Collisions and rebounds of chemically active droplets. *J. Fluid Mech.* **886**, A17.

MAASS, C.C., KRÜGER, C., HERMINGHAUS, S. & BAHR, C. 2016 Swimming droplets. *Annu. Rev. Condens. Matter Phys.* **7**, 171–193.

MALGARETTI, P., POPESCU, M.N. & DIETRICH, S. 2018 Self-diffusiophoresis induced by fluid interfaces. *Soft Matt.* **14** (8), 1375–1388.

MATSUDA, Y., SUEMATSU, N.J., KITAHATA, H., IKURA, Y.S. & NAKATA, S. 2016 Acceleration or deceleration of self-motion by the Marangoni effect. *Chem. Phys. Lett.* **654**, 92–96.

MEREDITH, C.H., CASTONGUAY, A.C., CHIU, Y.-J., BROOKS, A.M., MOERMAN, P.G., TORAB, P., WONG, P.K., SEN, A., VELEGOL, D. & ZARZAR, L.D. 2022 Chemical design of self-propelled Janus droplets. *Matter* **5** (2), 616–633.

MEREDITH, C.H., MOERMAN, P.G., GROENEWOLD, J., CHIU, Y.-J., KEGEL, W.K., VAN BLAADEREN, A. & ZARZAR, L.D. 2020 Predator–prey interactions between droplets driven by non-reciprocal oil exchange. *Nat. Chem.* **12** (12), 1136–1142.

MICHALET, X. 2010 Mean square displacement analysis of single-particle trajectories with localization error: Brownian motion in an isotropic medium. *Phys. Rev.* E **82** (4), 041914.

MICHELIN, S. 2023 Self-propulsion of chemically active droplets. *Annu. Rev. Fluid Mech.* **55**, 77–101.

MICHELIN, S. & LAUGA, E. 2015 Autophoretic locomotion from geometric asymmetry. *Eur. Phys.* J **38**, 1–16.

MICHELIN, S., LAUGA, E. & BARTOLO, D. 2013 Spontaneous autophoretic motion of isotropic particles. *Phys. Fluids* **25** (6), 061701.

MORAN, J.L. & POSNER, J.D. 2017 Phoretic self-propulsion. *Annu. Rev. Fluid Mech.* **49**, 511–540.

MOROZOV, M. & MICHELIN, S. 2019a Nonlinear dynamics of a chemically-active drop: from steady to chaotic self-propulsion. *J. Chem. Phys.* **150** (4), 044110.

MOROZOV, M. & MICHELIN, S. 2019b Self-propulsion near the onset of Marangoni instability of deformable active droplets. *J. Fluid Mech.* **860**, 711–738.

NAKATA, S., KIRISAKA, J., ARIMA, Y. & ISHII, T. 2006 Self-motion of a camphanic acid disk on water with different types of surfactants. *J. Phys. Chem.* B **110** (42), 21131–21134.

NASOURI, B. & GOLESTANIAN, R. 2020a Exact axisymmetric interaction of phoretically active Janus particles. *J. Fluid Mech.* **905**, A13.

NASOURI, B. & GOLESTANIAN, R. 2020b Exact phoretic interaction of two chemically active particles. *Phys. Rev. Lett.* **124** (16), 168003.

PALAGI, S., *et al.* 2016 Structured light enables biomimetic swimming and versatile locomotion of photoresponsive soft microrobots. *Nat. Mater.* **15** (6), 647–653.

PAXTON, W.F., KISTLER, K.C., OLMEDA, C.C., SEN, A., ST. ANGELO, S.K., CAO, Y., MALLOUK, T.E., LAMMERT, P.E. & CRESPI, V.H. 2004 Catalytic nanomotors: autonomous movement of striped nanorods. *J. Am. Chem. Soc.* **126** (41), 13424–13431.

PAXTON, W.F., SUNDARARAJAN, S., MALLOUK, T.E. & SEN, A. 2006 Chemical locomotion. *Angew. Chem. Intl Ed. Engl.* **45** (33), 5420–5429.

PEDDIREDDY, K., KUMAR, P., THUTUPALLI, S., HERMINGHAUS, S. & BAHR, C. 2012 Solubilization of thermotropic liquid crystal compounds in aqueous surfactant solutions. *Langmuir* **28** (34), 12426–12431.

PENG, G.G. & SCHNITZER, O. 2023 Weakly nonlinear dynamics of a chemically active particle near the threshold for spontaneous motion. II. History-dependent motion. *Phys. Rev. Fluids* **8** (3), 033602.

PICELLA, F. & MICHELIN, S. 2022 Confined self-propulsion of an isotropic active colloid. *J. Fluid Mech.* **933**, A27.

POPESCU, M.N., DIETRICH, S., TASINKEVYCH, M. & RALSTON, J. 2010 Phoretic motion of spheroidal particles due to self-generated solute gradients. *Eur. Phys. J.* E **31** (4), 351–367.

RAO, K.J., LI, F., MENG, L., ZHENG, H., CAI, F. & WANG, W. 2015 A force to be reckoned with: a review of synthetic microswimmers powered by ultrasound. *Small* **11** (24), 2836–2846.

SCHNITZER, O. 2023 Weakly nonlinear dynamics of a chemically active particle near the threshold for spontaneous motion: adjoint method. *Phys. Rev. Fluids* **8** (3), 034201.

SEEMANN, R., FLEURY, J.-B. & MAASS, C.C. 2016 Self-propelled droplets. *Eur. Phys.* J **225** (11), 2227–2240.

SHARIFI-MOOD, N., MOZAFFARI, A. & CÓRDOVA-FIGUEROA, U.M. 2016 Pair interaction of catalytically active colloids: from assembly to escape. *J. Fluid Mech.* **798**, 910–954.

SHIMOKAWA, M. & SAKAGUCHI, H. 2022 Hula-hoop-like motion and subcritical bifurcation of the rotation of an elliptical paper disk coated with camphor. *J. Phys. Soc. Japan* **91** (7), 074002.

SITTI, M., CEYLAN, H., HU, W., GILTINAN, J., TURAN, M., YIM, S. & DILLER, E. 2015 Biomedical applications of untethered mobile milli/microrobots. *Proc. IEEE* **103** (2), 205–224.

SONDAK, D., HAWLEY, C., HENG, S., VINSONHALER, R., LAUGA, E. & THIFFEAULT, J.-L. 2016 Can phoretic particles swim in two dimensions? *Phys. Rev.* E **94** (6), 062606.

SOTO, F., KARSHALEV, E., ZHANG, F., ESTEBAN FERNANDEZ DE AVILA, B., NOURHANI, A. & WANG, J. 2021 Smart materials for microrobots. *Chem. Rev.* **122** (5), 5365–5403.

SU, H., PRICE, C.-A.H., JING, L., TIAN, Q., LIU, J. & QIAN, K. 2019 Janus particles: design, preparation, and biomedical applications. *Mater. Today Bio* **4**, 100033.

SUDA, S., SUDA, T., OHMURA, T. & ICHIKAWA, M. 2021 Straight-to-curvilinear motion transition of a swimming droplet caused by the susceptibility to fluctuations. *Phys. Rev. Lett.* **127** (8), 088005.

SUEMATSU, N.J., IKURA, Y., NAGAYAMA, M., KITAHATA, H., KAWAGISHI, N., MURAKAMI, M. & NAKATA, S. 2010 Mode-switching of the self-motion of a camphor boat depending on the diffusion distance of camphor molecules. *J. Phys. Chem.* C **114** (21), 9876–9882.

SUEMATSU, N.J., SAIKUSA, K., NAGATA, T. & IZUMI, S. 2019 Interfacial dynamics in the spontaneous motion of an aqueous droplet. *Langmuir* **35** (35), 11601–11607.

SUGA, M., SUDA, S., ICHIKAWA, M. & KIMURA, Y. 2018 Self-propelled motion switching in nematic liquid crystal droplets in aqueous surfactant solutions. *Phys. Rev.* E **97** (6), 062703.

TANG, S., *et al.* 2020 Enzyme-powered Janus platelet cell robots for active and targeted drug delivery. *Sci. Robot.* **5** (43), eaba6137.

THUTUPALLI, S., GEYER, D., SINGH, R., ADHIKARI, R. & STONE, H.A. 2018 Flow-induced phase separation of active particles is controlled by boundary conditions. *Proc. Natl Acad. Sci. USA* **115** (21), 5403–5408.

THUTUPALLI, S. & HERMINGHAUS, S. 2013 Tuning active emulsion dynamics via surfactants and topology. *Eur. Phys. J.* E **36** (8), 1–10.

TOMLINSON II, C. 1862 On the motions of camphor on the surface of water. *Proc. R. Soc. Lond.* **11**, 575–577.

VAN OOSTEN, C.L., BASTIAANSEN, C.W.M. & BROER, D.J. 2009 Printed artificial cilia from liquid-crystal network actuators modularly driven by light. *Nat. Mater.* **8** (8), 677–682.

VYSKOCIL, J., MAYORGA-MARTINEZ, C.C., JABLONSKA, E., NOVOTNY, F., RUML, T. & PUMERA, M. 2020 Cancer cells microsurgery via asymmetric bent surface Au/Ag/Ni microrobotic scalpels through a transversal rotating magnetic field. *ACS Nano* **14** (7), 8247–8256.

WENTWORTH, C.M., CASTONGUAY, A.C., MOERMAN, P.G., MEREDITH, C.H., BALAJ, R.V., CHEON, S.I. & ZARZAR, L.D. 2022 Chemically tuning attractive and repulsive interactions between solubilizing oil droplets. *Angew. Chem. Intl Ed. Engl.* **61** (32), e202204510.

YANG, Q., JIANG, M., PICANO, F. & ZHU, L. 2023 Shaping active matter: from crystalline solids to active turbulence. arXiv:2304.01593.

YARIV, E. 2017 Two-dimensional phoretic swimmers: the singular weak-advection limits. *J. Fluid Mech.* **816**, R3.

YARIV, E. & KAYNAN, U. 2017 Phoretic drag reduction of chemically active homogeneous spheres under force fields and shear flows. *Phys. Rev. Fluids* **2** (1), 012201.